

Load bearing capacity of tool pin during friction stir welding

A. Arora · M. Mehta · A. De · T. DebRoy

Received: 10 March 2011 / Accepted: 7 November 2011
© Springer-Verlag London Limited 2011

Abstract Although friction stir welding (FSW) is now widely used for the welding of aluminum and other soft alloys, premature tool failure limits its application to hard alloys such as steels and titanium alloys. The tool pin, the weakest component of the tool, experiences severe stresses at high temperatures due to both bending moment and torsion. It is shown that the optimum tool pin geometry can be determined from its load bearing capacity for a given set of welding variables and tool and work-piece materials. The traverse force and torque during friction stir welding are computed using a three-dimensional heat transfer and viscoplastic material flow model considering temperature and strain rate-dependent flow stress of the work-piece material. These computed values are used to determine the maximum shear stress experienced by the tool pin due to bending moment and torsion for various welding variables and tool pin dimensions. It is shown that a tool pin with smaller length and larger diameter will be able to sustain more stress than a longer pin with smaller diameter. The proposed methodology is used to explain the failure and deformation of the tool pin in independent experiments for the welding of both L80 steel and AA7075 alloy. The results demonstrate that the short tool life in a typical FSW of steels is contributed by low values of factor of safety in an environment of high temperature and severe stress.

Keywords Friction stir welding · Tool pin · Aluminum alloys · Steel

1 Introduction

Friction stir welding (FSW) typically involves the linear motion of a rotating tool that heats the work-piece, mostly by friction. The softened material moves around the tool and forms a joint behind it. Since FSW does not involve bulk melting, the common problems of fusion welding such as solidification and liquation cracking, porosity and loss of volatile alloying elements can be prevented. Because of these advantages, FSW has been widely used to join aluminum alloys and other soft materials. However, the FSW tool is subjected to severe stress and wear at high temperatures, especially for the welding of steels and other hard alloys such as the titanium alloys. The relatively short tool life now limits the commercial application of FSW to steels and titanium alloys. Development of reusable tools remains the most important challenge in the expanded application of FSW.

Typically, an FSW tool consists of a round shoulder and a structurally weaker cylindrical threaded pin. The tool pin experiences severe bending moment and torsion due to the continuous linear and rotational motions through the work-piece. Currently, the tools are designed by trial and error and there is no systematic study to examine the mechanical behavior of the tools under the conditions of FSW. It will be shown subsequently in this paper that FSW tools are sometimes used with a very small factor of safety. Since most tool failures occur due to the failure of tool pin, improved understanding of the mechanical behavior of the pin under the conditions of FSW is needed.

A. Arora (✉) · T. DebRoy
Department of Materials Science and Engineering,
The Pennsylvania State University,
University Park, PA, USA
e-mail: amitarora@psu.edu

M. Mehta · A. De
Department of Mechanical Engineering, IIT,
Mumbai, India

The material flow and weld joint properties during FSW are affected by the tool pin geometries and have been studied by several researchers [1–17]. Bhadeshia and DebRoy [1] have highlighted the inadequacy of the commonly used tool materials for FSW of steels. Nandan et al. [2] have reviewed FSW of several alloys and the commonly used tools. Hirasawa et al. [3] used particle method to understand the effect of tool geometry on plastic flow during friction stir spot welding. Elangovan and Balasubramanian [4] studied the formation of friction stir processing zone for various tool pin profiles and showed that the tool with square pin profile resulted in defect-free welds irrespective of the welding speeds. Hattingh et al. [5] showed that defect-free welds could be made using a tri-fluted tapered pin considering a relation between the thread pitch, the pin diameter, and the plate thickness. Badarinarayan et al. [6] showed the effect of tool geometry on the strength of the friction stir spot welds for AA5754-O. They [6] studied the hook formation during friction stir spot welding to explain the higher static strength for welds made with triangular pin compared to the same for welds made with circular pins. Tozaki et al. [7] used different tool pin lengths to study the effect on microstructure and static strength in friction stir spot welding of AA5083. Thomas et al. [8] and, subsequently, Thomas [9] suggested new tool pin designs for improved material flow and higher heat generation. Zhao et al. [10, 11] showed that use of a threaded tapered tool pin would lead to minimum defects in AA2014 welds. Buffa et al. [12] have shown that the peak temperature increases with increase in the pin taper angle. Fujii et al. [13] obtained defect-free welds of AA1050 using a threadless columnar pin and of AA5083 using a triangular prism shaped pin. Kumar and Kailas [14] suggested that the material flow due to the tool pin would affect the formation of defects in welds. Colegrove and Shercliff [15, 16] used a mathematical model to show that the Triflute pin increased the downward material flow. Colegrove and Shercliff [17] have also used a model to estimate the traverse force during FSW. However, the model predictions of tool force were one order of magnitude lower than those measured in an independent experiment. They [17] suggested that better agreement between the experimental and the computed values could be achieved by reducing the flow of materials around the tool either by considering appropriate slip between the tool and the material or by viscosity softening near the solidus. In summary, although the available research has examined the effects of pin geometries on the material flow, its effects on the bending and shear stresses experienced by the tool pin have not been addressed. Since real-time measurement of the stresses experienced by the tool pin is difficult, a recourse is to use a reliable mathematical model. Sorensen and Stahl [18] proposed a relationship to calculate pin force based on regression analysis of the measured experimental data for the FSW of AA6061. They [18]

suggested that the relationship was valid for tool pins of 5.6 mm or shorter.

In recent times, heat transfer and material flow models of FSW are used extensively to realize the influence of tool shoulder diameter on the peak temperature, torque, and power requirements [19, 20]. Furthermore, the optimum tool shoulder diameter can now be computed for a given set of process variables in FSW based on a balance between the need to soften the material and for the tool to have a good grip on the plasticized material [19, 20]. The influence of the pin dimensions on the stress experienced by the tool pin considering its load bearing capacity has not been analyzed. Such an analysis would be of significant value for the determination of suitable tool pin dimensions based on scientific principles.

A methodology is proposed and tested here to compute the traverse force experienced by the tool for various welding conditions and tool geometries for the FSW of AA2024, AA6061, and Ti–6Al–4V alloys. The computed values of force and torque on the tool pin are used to compute the maximum shear stress experienced by the tool pin due to a combined action of bending and torsion. It is shown that suitable tool pin dimensions can be determined from its load bearing ability for a given set of tool material and welding conditions. The model is also used to explain the failure and deformation of tool pin during FSW of AA7075 and L80 steel reported in independent literature.

2 Numerical model

The tool pin experiences stresses due to bending and torsion because of the linear and rotational motion, respectively. A typical force distribution, $q(z)$, on a straight cylindrical FSW tool pin is shown schematically in Fig. 1a. The force distribution, $q(z)$, is opposite to the welding direction. A transverse cross-section of the tool pin along S–S in Fig. 1a is shown in Fig. 1b. The bending moment, M_y , at a point A in Fig. 1b can be computed as [21]:

$$M_y = \int_{z_1}^L z q(z) dz \quad (1)$$

where L is the length of pin, z_1 is the distance of the point A from the root of the pin, $q(z)$ is the force on the infinitesimal part of the pin dz at $(z+z_1)$ distance from the root of the pin. The normal stress due to bending, σ_B , is calculated as [21]:

$$\sigma_B = \frac{M_y x}{I_{yy}} = \frac{M_y (r \cos \theta)}{\pi r^4 / 4} = \frac{4 \cos \theta}{\pi r^3} \int_{z_1}^L z q(z) dz \quad (2)$$

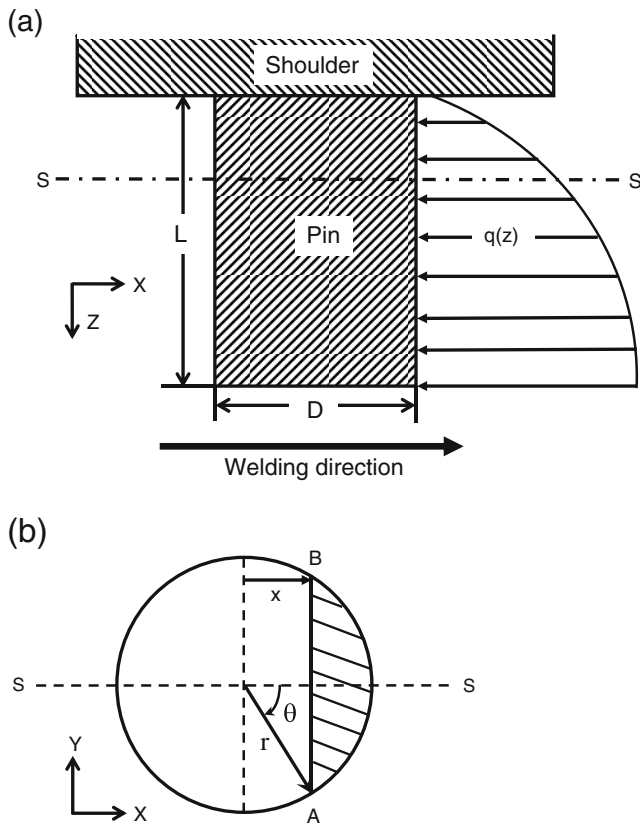


Fig. 1 Schematic layout of a straight cylindrical pin and **b** cross-section along S-S

where x is the normal distance of the cord AB from the neutral axis of the pin, I_{yy} is the second moment of area, r is the radius of the pin, and θ is the angle of the point A from the welding direction. The shear stress, τ_T , at point A due to torsion can be estimated as [21]:

$$\tau_T = \frac{M_T r}{J_{zz}} = \frac{M_T r}{\pi r^4 / 2} \tag{3}$$

where M_T is the sticking torque experienced at point A and J_{zz} is the polar moment of area. Since the length-to-diameter ratio of the pin is less (<20), the shear stress, τ_B , due to bending needs to be considered. [21] The calculation of τ_B requires an estimate of shear force, V , and of Q , the

first moment of area of the section beyond chord AB (Fig. 1b) about neutral axis (y -axis). The terms V and Q are computed, respectively, as [21]:

$$V = \int_{z_1}^L q(z) dz \tag{4}$$

$$Q = \int_x^r gx dx \tag{5}$$

where g is the length of the chord AB and $g = 2\sqrt{r^2 - x^2}$. Thus, $x dx = -(g dg)/4$ and since $x = r \cos \theta$, Q is rewritten as:

$$Q = \int_g^0 g \left(-g \frac{dg}{4} \right) = \int_0^g \frac{g^2}{4} dg = \frac{g^3}{12} = \frac{(2\sqrt{r^2 - x^2})^3}{12} = \frac{2}{3} (r \sin \theta)^3 \tag{6}$$

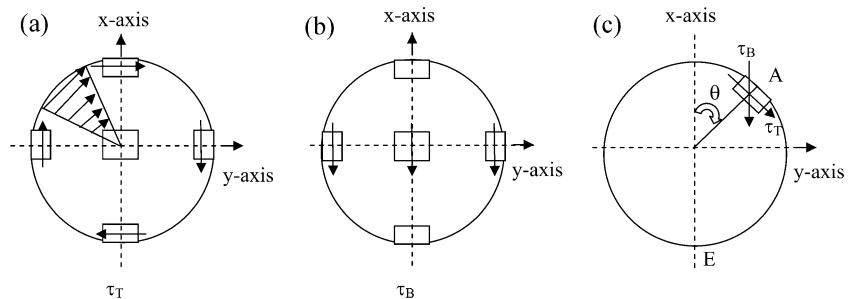
The shear stress, τ_B , at point A due to bending can now be computed as [21]:

$$\tau_B = \frac{VQ}{I_{yy}g} = \frac{4}{3} \frac{\sin^2 \theta}{\pi r^2} \int_{z_1}^L q(z) dz \tag{7}$$

Figure 2a, b schematically show the typical nature of distribution at several locations on the section SS in Fig. 1b, respectively. Figure 2c indicates the distribution of τ_T and τ_B at any element located at point A. The maximum and minimum principal stresses, σ_1 and σ_2 , respectively, at point A due to combined bending and torsion loading can be written as [21]:

$$\sigma_{1,2} = \frac{\sigma_B}{2} \pm \sqrt{\left(\frac{\sigma_B}{2}\right)^2 + (\tau_B + \tau_T \sin \theta)^2 + (\tau_T \cos \theta)^2} \tag{8}$$

Fig. 2 Schematic illustrations of τ_T and τ_B at section S-S and of τ_T and τ_B at point A



Following Tresca’s criteria, the maximum shear stress, τ_{\max} , at A will be obtained as [21]:

$$\tau_{\max} = \frac{\sigma_1 - \sigma_2}{2} = \sqrt{\left(\frac{\sigma_B}{2}\right)^2 + (\tau_B + \tau_T \sin \theta)^2 + (\tau_T \cos \theta)^2} \quad (9)$$

Equation 9 provides an estimate of the maximum shear stress that any point on the tool pin is expected to bear during FSW. To compute the maximum shear stress, the force distribution, $q(z)$, and torque, M_T , on the tool pin need to be calculated. A three-dimensional heat transfer and visco-plastic flow model for FSW is used to compute the torque and force values. The model solves the conservation equation of mass, momentum, and energy in a steady-state, three-dimensional Cartesian coordinate considering incompressible single-phase flow. The energy conservation equation is solved in a moving coordinate system and given as [22–28]:

$$\rho C_p \frac{\partial(u_i T)}{\partial x_i} = -\rho C_p U_1 \frac{\partial T}{\partial x_1} + \frac{\partial}{\partial x_i} \left(k \frac{\partial T}{\partial x_i} \right) + S_{in} + S_b \quad (10)$$

where ρ is the density of the material, C_p and k are the temperature-dependent specific heat and thermal conductivity of the material, respectively, u_i is the velocity component, T is the temperature, U_1 is the welding velocity, and S_{in} and S_b are the source terms due to rate of interfacial heat generation per unit volume at the tool–work-piece interface and rate of heat generation due to plastic deformation in work-piece material, respectively. The rate of heat generation at the tool–work-piece interface is defined as [24–28]:

$$S_{in} = [(1 - \delta)\eta\tau + \delta\mu P](\omega r - U_1 \sin \theta) \quad (11)$$

where δ and μ are spatially variable fractional slip and coefficient of friction, respectively, between the tool and the work-piece, η is the mechanical efficiency, τ is the shear stress at yielding, ω is the tool rotation speed, r is the radial distance from the tool axis, and θ is the angle with the direction of movement of the tool. The term $\omega r - U_1 \sin \theta$ represents the local velocity of a point on the tool with the origin fixed at the tool axis. The spatial variations of fractional slip, δ , and the coefficient of friction, μ , in Eq. 11 are derived from the trend of the reported data on accumulated slip during cross-wedge rolling as [29]:

$$\delta = 0.31 \times \exp\left(\frac{\omega r}{1.87}\right) - 0.026 \quad (12)$$

$$\mu = 0.5 \times \exp(-\delta\omega r) \quad (13)$$

where ωr is in m/s. Equations 12 and 13 are valid for ωr from 0.1 to 1.6 m/s [29]. The rate of heat generation due to plastic deformation, S_b , is computed as $\lambda\mu_v\dot{\epsilon}^2$ where μ_v is

dynamic viscosity, $\mu_v\dot{\epsilon}^2$ refers to plastic work done with $\dot{\epsilon}$ as the effective strain rate, and λ depicts the extent of mixing of deforming materials on the atomic scale. The spatially variable strain rate $\dot{\epsilon}$ is computed as follows:

$$\dot{\epsilon} = \sqrt{\frac{2}{3} \left(\left(\frac{\partial u_i}{\partial x_i} \right)^2 + \frac{1}{2} \left(\frac{\partial u_1}{\partial x_2} + \frac{\partial u_2}{\partial x_1} \right)^2 + \frac{1}{2} \left(\frac{\partial u_1}{\partial x_3} + \frac{\partial u_3}{\partial x_1} \right)^2 + \frac{1}{2} \left(\frac{\partial u_3}{\partial x_2} + \frac{\partial u_2}{\partial x_3} \right)^2 \right)} \quad (14)$$

where u_i is the velocity component with $i=1, 2$ and 3 referring to the three axes in the Cartesian coordinate system. The torque (M) required during FSW is computed as [19, 20]:

$$M = M_T + M_L \quad (15)$$

where M_T and M_L are the sticking and sliding components of the total torque, respectively. The values of M_T and M_L are computed as follows [19, 20]:

$$M_T = \oint_A r_A \times (1 - \delta)\tau \times d_A \quad (16)$$

$$M_L = \oint_A r_A \times \delta\mu P \times d_A \quad (17)$$

where r_A is the distance of any infinitesimal area element, dA , δ is the spatial fractional slip, μ is the coefficient of friction, P is the normal pressure, and τ is the temperature-dependent shear strength. The temperature and material flow required for determination of the shear strength of the deforming material during friction stir welding is computed using a three-dimensional heat transfer and viscoplastic flow model [19, 20, 22–28]. The details about the model are not relevant to the work presented here and thus are not provided. The tool traverse force (F) on the tool during FSW is computed as:

$$F = F_S + F_P \quad (18)$$

where F_S and F_P refer to the force components experienced by the shoulder and the pin, respectively. The values of F_S and F_P are computed as:

$$F_S = \oint_A \delta \times \mu P \times d_A \quad (19)$$

$$F_P = \oint_A \sigma \times d_A \quad (20)$$

where σ is the temperature-dependent yield strength of the deforming material and d_A is the projected contact area of the tool pin.

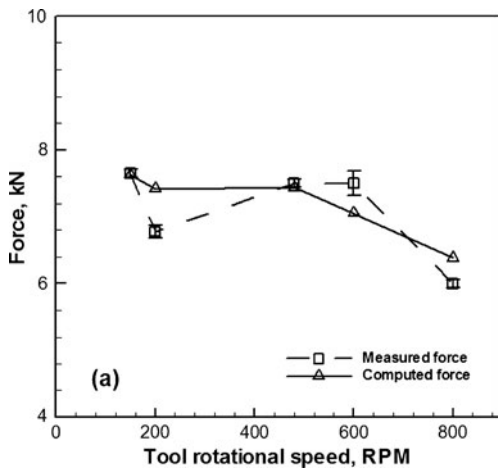


Fig. 3 A comparison of the experimental and computed traverse force values as a function of tool rotational speed during FSW of AA2524 at the welding speed of 2.11 mm/s [30]

3 Results and discussions

Figures 3 and 4 show the computed and the corresponding experimentally measured values of tool traverse force obtained from independent experiments [30, 31] for FSW of AA2524 and Ti-6Al-4V alloys, respectively. In Fig. 3, the welding velocity and the plunge force are constant at 2.11 mm/s and 42.3 kN, respectively, for all the cases, while the rotational speed varies from 150 to 800 RPM. The computed values of traverse force decreases with increase in tool rotational speed. The faster rotation of the tool results in greater rate of heat generation and softening of the work-piece. Figure 4 depicts the computed and the corresponding measured traverse forces during FSW of Ti-6Al-4V alloy at different combinations of rotational speed, plunge force and welding speed. The specific values of these variables are given in Table 1. The error bars for

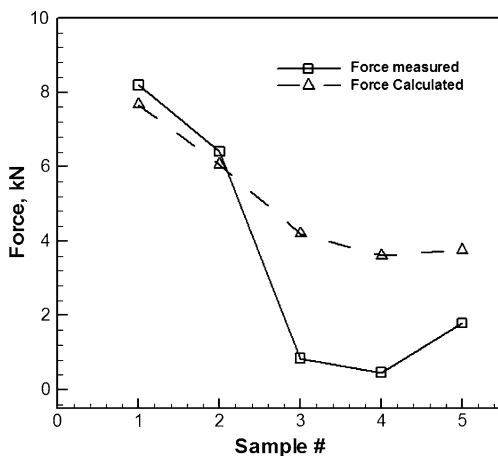


Fig. 4 A comparison of the computed and corresponding experimentally measured total traverse force for FSW of Ti-6Al-4V alloy. The welding conditions for the five samples are given in Table 1 [31]

Table 1 Experimentally measured and corresponding computed values of tool traverse force during FSW of Ti-6Al-4V alloy at different welding conditions

Data set index	RPM	Welding speed (mm/s)	Plunge force (kN)	Tool traverse force (kN)	
				Measured	Computed
1	120	0.85	32.920	8.200	7.663
2	150	0.85	21.320	6.410	6.060
3	200	0.85	9.050	0.849	4.196
4	400	1.70	6.220	0.471	3.613
5	800	3.40	9.620	1.792	3.759

experimental values shown in Fig. 3 are one standard deviation as reported in the literature [30]. No information about the measurement or statistical error was available in the reported literature for the experimental values in Fig. 4. Figure 4 indicates that the tool traverse force reduces with increase in rotational speed and also with decrease in plunge force (cases #1, #2 and #3) at a constant welding speed. The increase in plunge force leads to greater friction force on the tool shoulder, resulting in increase in traverse force. For higher rpm runs, cases #4 and #5 in Table 1, the traverse force increases due to the increase in the plunge force and increase in welding speed. The increased welding speed reduces the amount of heat generated per unit length of the weld and, as a result, the material is not adequately softened, leading to greater traverse force. However, the effect of higher welding speed is also accompanied by the higher tool rotational speeds for these two cases and the measured forces are the combined effects of the two welding speed and the tool rotational speed.

Figures 5 and 6 show the computed and the corresponding measured values [18] of the tool traverse force as functions of

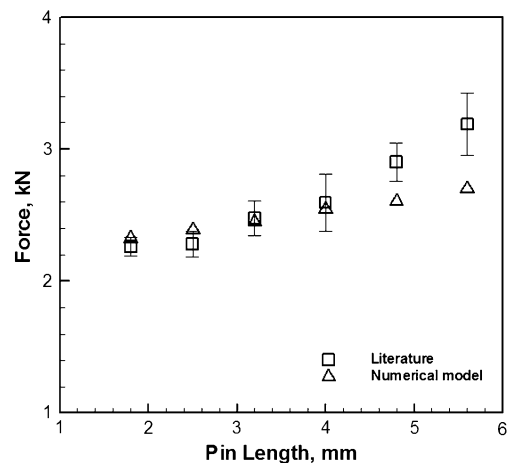


Fig. 5 A comparison of experimentally measured and corresponding computed total traverse force as a function of the pin length for the FSW of AA6061. The welding velocity is 3.33 mm/s, tool rotational speed is 650 RPM, and the pin diameter is 7.6 mm [18]

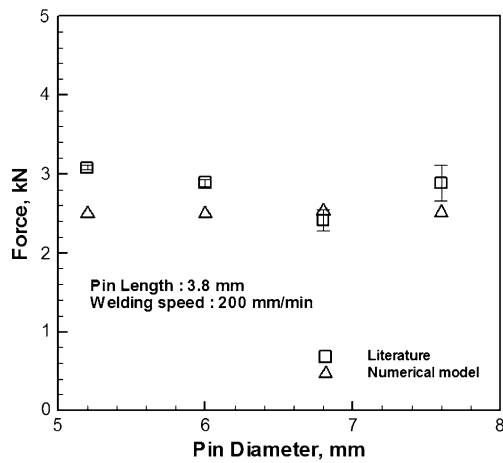


Fig. 6 A comparison of the computed and corresponding experimentally measured total traverse force for FSW of AA6061 as a function of pin diameter [18]. The welding velocity is 3.33 mm/s, the tool rotational speed is 650 RPM, and the pin length is 3.8 mm [18]

pin length and diameter, respectively, during FSW of AA6061 alloy with a rotational speed of 650 rpm and welding speed of 3.33 mm/s. The estimated errors in the experimentally measured values as reported in the original article are shown in Figs. 5 and 6. For a given plate thickness, the tool traverse force increases with increase in the pin length, while it remains nearly unaffected with change in pin diameter. Since most of the heat is generated at the shoulder–work-piece interface, the work-piece temperature decreases from the top to the bottom of the tool. The longer pin faces more work-piece material with lower temperature and higher flow stress towards its free end, resulting in higher traverse force. An increase in pin diameter has much lower influence on the softening of the work-piece material and allows only a marginal increase in interaction between the tool pin and

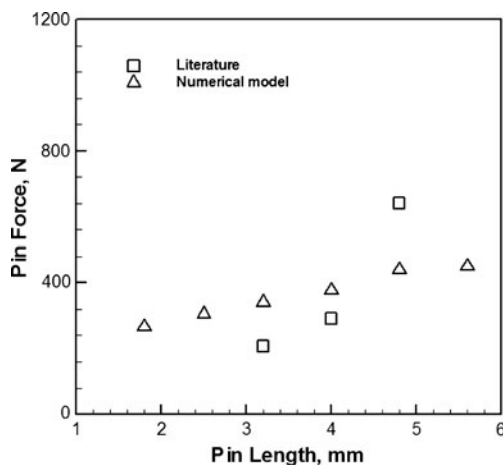


Fig. 7 A comparison of the force on the tool pin computed and the estimated values based on regression analysis model [18] for different pin lengths. The welding velocity is 3.33 mm/s, the tool rotational speed is 650 RPM, and the pin diameter is 7.6 mm [18]

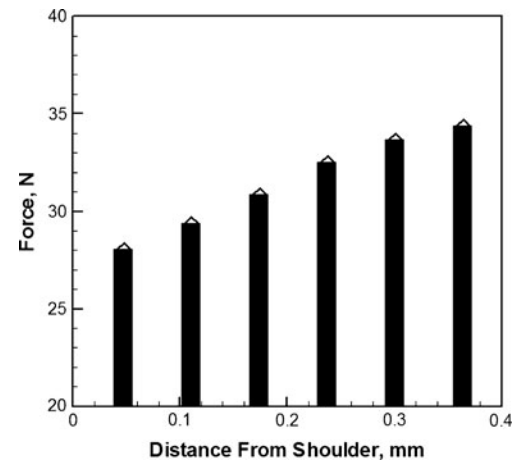


Fig. 8 Typical distribution of traverse force from the root to the tip of a tool pin for a given pin geometry. The welding velocity is 3.33 mm/s, the tool rotational speed is 650 RPM, the pin diameter is 7.6 mm, and the pin length is 3.8 mm

work-piece. Thus, the pin length has a stronger influence on the computed traverse force than the pin diameter. Figures 3, 4, 5 and 6 show a fair agreement between the computed and the corresponding experimentally measured values of the traverse force for various welding conditions, tool dimensions and different work-piece materials.

Figure 7 shows the numerically computed values of pin force from Eq. 20 as a function of tool pin length. The results show that the pin force increases gradually with increase in pin length as expected. The force acting on the tool pin cannot be obtained easily from the experimentally determined values of the total tool force. However, the values of pin force allow us to understand the thermomechanical environment experienced by the tool pin during FSW. This is particularly important because failure of the FSW tool often occurs due to

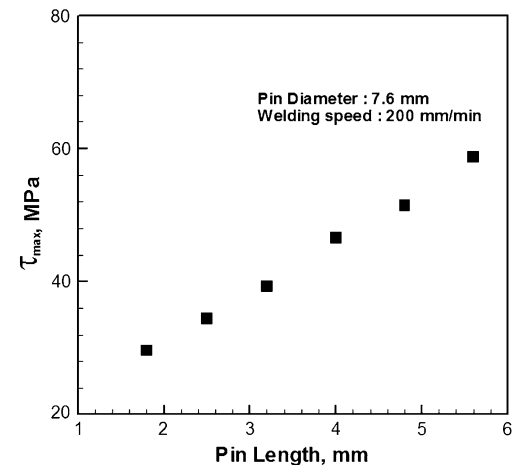


Fig. 9 The computed maximum shear stress (τ_{max}) on the tool pin as a function of the pin length during FSW of AA6061. The welding velocity is 3.33 mm/s, the tool rotational speed is 650 RPM, and the pin diameter is 7.6 mm

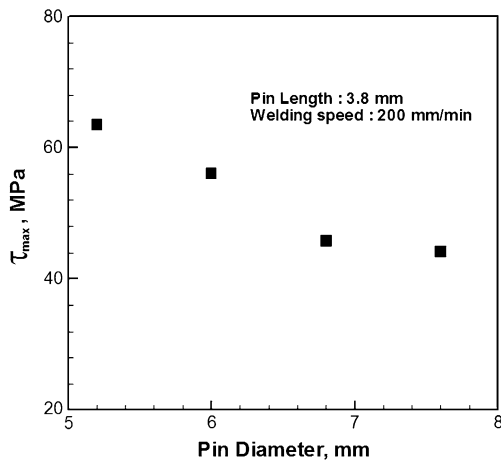


Fig. 10 The computed maximum shear stress (t_{max}) on the tool pin as a function of the pin diameter during FSW of AA6061. The welding velocity is 3.33 mm/s, the tool rotational speed is 650 RPM, and the pin length is 3.8 mm

the failure of the pin. Sorensen and Stahl [18] proposed a regression-based model to estimate the pin force values for the FSW of AA6061 for pin lengths between 2.5 and 5.5 mm. The values of pin force estimated using their regression equation are also shown in the same figure. The order of magnitude of these values is comparable to the numerically computed values of tool pin force. However, there are some differences in the values of the pin force. It should be recognized that the tool pin force was not measured experimentally [18], instead its values were estimated from the measured values of the total force on the FSW tool. The total force values computed using our numerical model shows good agreement with their measured values as shown in Fig. 5.

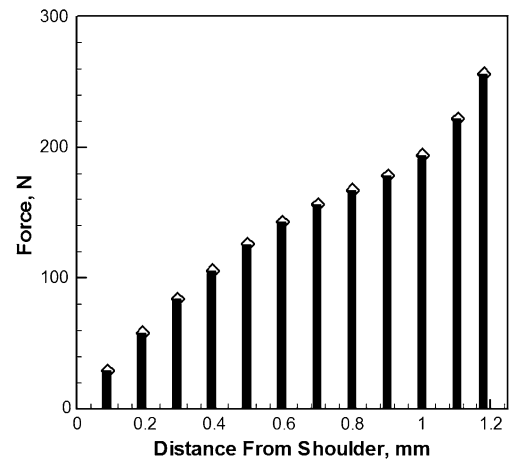


Fig. 11 The force distribution on the tool pin during FSW of L80 steel. The welding velocity is 1.7 mm/s and the tool rotational speed is 170 RPM [33]

Figure 8 shows the computed distribution of traverse force from the root to the tip along the pin length during FSW of AA6061 with pin diameter and length of 7.6 and 3.8 mm, respectively, at a welding speed of 3.33 mm/s and tool rotational speed of 650 RPM. A continuous increase in the pin traverse force from the root towards the tip is clear in Fig. 8. Since the deforming material away from the shoulder is at lower temperatures, the flow stress of the material is higher. The tool pin experiences greater resistance to motion near the tip than near the root. A tool pin is structurally similar to a cantilever beam with one end fixed to the tool shoulder. The distribution of traverse force, as shown in Fig. 8, leads to a bending moment on the pin resulting in bending (σ_B) and shear stresses (τ_B) along and perpendicular to the axis of the pin, respectively. In

Table 2 The tool material, dimensions, and welding variables used for calculation of force and torque

Work-piece material	AA2524	Ti-6Al-4V	AA-6061	L80 Steel	AA 7075
Tool material	Steel	Tungsten	H13 tool steel	Commercially pure tungsten	H13 tool steel
Tool shoulder diameter, mm	20.3	25.0	25.4	35.0	26.4
Pin diameter at root, mm	7.1	19.8	5.2–7.6	20.0	5.2
Pin diameter at tip, mm	7.1	0.2	5.2–7.6	20.0	1.5
Pin length, mm	6.2	9.9	1.8–5.6	12.0	5.1
Work-piece thickness, mm	6.4	10.3	9.5	12.7	6.0
Tool rotational speed, RPM	150–800	120–800	650	170	800
Welding speed, mm/s	2.11	0.85–3.4	3.33	1.7	2.1
Axial pressure, MPa	130.7	40–137	20.0	92.5	20.0
*Specific heat, J kg ⁻¹ K ⁻¹	$25.82 + 0.38 T + 2.9 \times 10^{-5} T^2 + 2.7 \times 10^{-7} T^3$	$628.03 - 3.93 \times 10^{-1} T + 5.95 \times 10^{-4} T^2$	$9.29 \times 10^2 - 6.27 \times 10^{-1} T + 1.48 \times 10^{-3} T^2 - 4.33 \times 10^{-8} T^3$	$3.30 \times 10^2 \times \exp(9.56 \times 10^{-4} T)$	$853.5 - 1.25 T + 4.18 \times 10^{-4} T^2 - 1.25 \times 10^{-8} T^3$
Thermal conductivity ^a , W m ⁻¹ K ⁻¹	$929.3 - 6.2 \times 10^{-1} T - 1.4 \times 10^{-3} T^2 + 4.3 \times 10^{-8} T^3$	$4.44 + 4.33 \times 10^{-3} T + 1.05 \times 10^{-5} T^2$	$2.52 \times 10^1 + 3.98 \times 10^{-1} T + 7.36 \times 10^{-6} T^2 - 2.52 \times 10^{-7} T^3$	$47.28 - 4.18 \times 10^{-2} T + 1.05 \times 10^{-4} T^2 - 4.6 \times 10^{-8} T^3$	$74.52 + 2.5 \times 10^{-1} T - 4.2 \times 10^{-5} T^2$

^a Temperature, T , in K

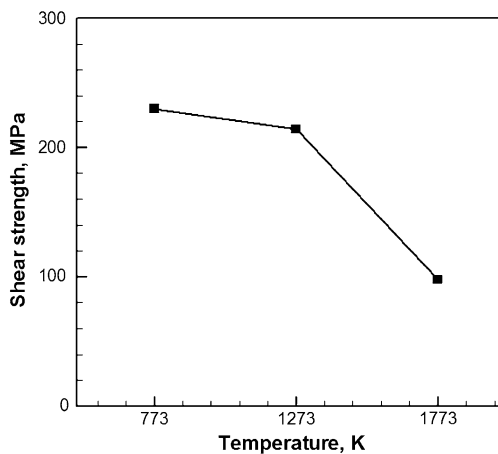


Fig. 12 Temperature-dependent shear strength of the commercially pure tungsten as reported by Kravchenko et al. [34]

addition, the pin will experience shear stress (τ_T) due to the traction of the work-piece material during tool rotation. An estimation of the resultant stress acting on the tool pin will provide a measure of its load bearing capacity during FSW. The maximum shear stress, τ_{MAX} , acting at any point on the surface of a tool pin with circular cross-section can be computed as shown in Eq. 9.

Figures 9 and 10 show the computed values of τ_{MAX} at the root of the tool pin as a function of the length and diameter of the tool pin. As the length of the pin increases, a larger part of the pin along the tool axis faces work-piece material with lesser temperature. Thus, the tool pin force increases with increase in the tool pin length, leading to increase in the computed values of τ_{MAX} . Therefore, longer pin length with a constant pin diameter would require stronger tool material for sustainable performance. Figure 10 shows that the maximum shear stress experienced by the tool pin decreases as the tool pin diameter increases. The tool pin with larger diameter would be able to sustain greater bending and torsion moments for a constant pin length. The maximum shear stress experienced by the tool pin is in the range of 29–65 MPa, which confirms to a factor of safety of



Fig. 13 The tools used by Neilsen during FSW of AA7075 after use. The tool pin in the second tool from the left sheared off during welding [35]

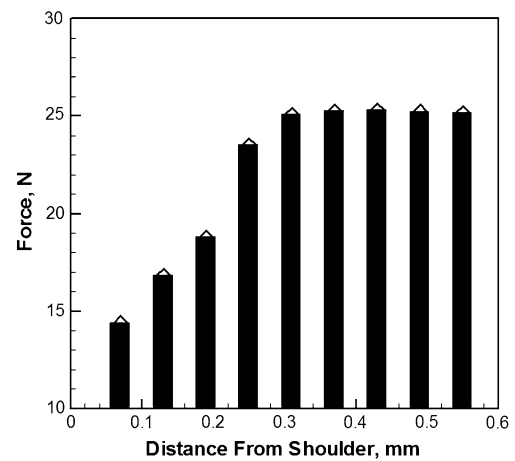


Fig. 14 The force distribution of the tool pin during FSW of AA7075 alloy. The tool rotational speed is 800 RPM and the welding speed is 4.66 mm/s

14 considering the shear strength of H13 tool steel at the corresponding temperature [32] for the FSW of AA6061.

Gan et al. [33] showed that the commercially pure tungsten tool used during FSW of L80 steel plates deformed and had significant reduction in length. The tool dimensions and the welding parameters shown in Table 2 are used to compute the torque and force on the tool pin. Figure 11 shows the force distribution on the tool pin as a function of the distance from the pin root. The force on the tool pin increases as the distance from the root of the pin as expected. The computed force distribution on tool pin and the torque are used to compute the maximum shear stress, τ_{MAX} , on the tool pin. The computed value of τ_{MAX} experienced by the tool pin at its root is 85 MPa. The peak temperature during FSW is reported to be approximately 1,273 K. The shear strength of tungsten at this temperature is about 214 MPa as shown in Figure 12 [34]. Thus, the FSW tool in this case is operating at a low factor of safety,

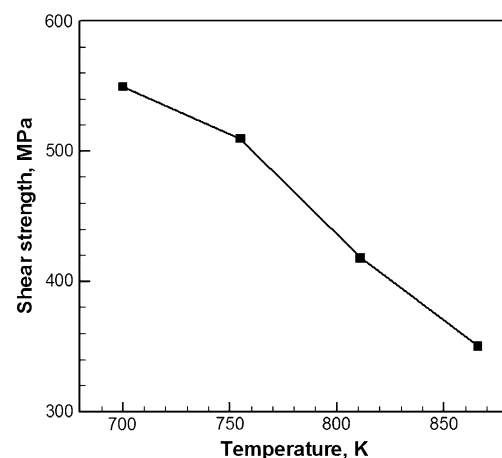


Fig. 15 The temperature-dependent shear strength of the H13 tool steel [32]

approximately 2.5 (~214/85), which is much smaller than that used during FSW of AA6061 considered previously. As shown by Gan et al. [33], the tool pin experienced severe deformation and approximately 12.5% reduction in pin length.

Nielsen [35] studied the effect of tool geometry on performance of a friction stir processing tool during FSW of AA7075 alloy. The convex scrolled shoulder step spiral (CS4) tools used by Nielsen [35] were made of H13 tool steel. Figure 13 shows that one of the tool pins sheared off at its mid-height during FSW. The welding variables used in the experiments are given in Table 2. Figure 14 shows the numerically computed force distribution on the tool pin as a function of the distance from the root of the tool pin. The maximum shear stress on the tool pin computed at its mid-length is 488 MPa. Figure 15 shows the shear strength of H13 tool steel as a function of temperature. The computed approximate peak temperature during FSW of AA7075 is 720 K and, at this temperature, the shear strength of H13 tool steel is 534 MPa (Fig. 15). Thus, the FSW tool is used with a safety factor of approximately 1.1 (~534/488). The use of FSW tool with such low safety factor made it susceptible to failure during welding of AA7075.

4 Conclusions

A three-dimensional heat transfer and visco-plastic model is used to compute the influence of pin length and diameter on traverse force during FSW. The total traverse force increases significantly with increase in pin length. The traverse force is insensitive to the pin diameter for the welding conditions considered here. A methodology based on the principles of load bearing capacity of a short cantilever beam is proposed to estimate the maximum shear stress on the tool pin due to a combined bending moment and torsion. The computed values of maximum shear stress on tool pin increases with either the increase in pin length or the decrease in pin diameter. In case of a typical literature reported deformation and failure of tool pin during FSW of L80 steel, the proposed methodology has shown that the maximum shear stress experienced by the tool pin would be very close to the shear strength of tool material. For the reported failure of tool pin during FSW of AA7075, the methodology shows that the shear strength of the tool material at the corresponding temperature is less than 1.1 times the maximum shear stress experienced by the tool pin. This explains the failure of the tool pin under the applied stresses. The short FSW tool life in this case can be contributed to a low value of factor of safety that can be considered as the ratio between the maximum shear stress on the tool pin under the applied stress and shear strength of the tool material at the working temperature. The proposed model

in combination with an appropriate factor of safety will be useful to prescribe suitable tool pin geometries for a given tool material and welding conditions.

References

- Bhadeshia HKDH, DebRoy T (2009) Critical assessment: friction stir welding of steels. *Sci Technol Weld Join* 14:193–196
- Nandan R, DebRoy T, Bhadeshia HKDH (2008) Recent advances in friction stir welding—process, weldment structure and properties. *Prog Mater Sci* 53:980–1023
- Hirasawa S, Badarinarayan H, Okamoto K, Tomimura T, Kawanami T (2010) Analysis of effect of tool geometry on plastic flow during friction stir spot welding using particle method. *J Mater Process Technol* 210:1455–1463
- Elangovan K, Balasubramanian V (2008) Influence of tool pin profile and welding speed on the formation of friction stir processing zone in AA2219 aluminum alloy. *J Mater Process Technol* 200:163–175
- Hattingh DG, Bignaut C, Niekerk TI, James MN (2008) Characterization of the influences of FSW tool geometry on welding forces and weld tensile strength using an instrumented tool. *J Mater Process Technol* 203:46–57
- Badarinarayan H, Shi Y, Li X, Okamoto K (2009) Effect of tool geometry on hook formation and static strength of friction stir spot welded aluminum 5754-O sheets. *Int J Mach Tools Manuf* 49:814–823
- Tozaki Y, Uematsu Y, Tokaji Y (2007) Effect of tool geometry on microstructure and static strength in friction stir spot welded aluminum alloys. *Int J Mach Tools Manuf* 47:2230–2236
- Thomas WM, Johnson KL, Wiesner CS (2003) Friction stir welding—recent developments in tool and process technologies. *Adv Eng Mater* 5:485–490
- Thomas WM (2003) Friction stir welding—recent developments. *Mater Sci Forum* 426–4:229–236
- Zhao YH, Lin SB, Wu L, Qu FX (2005) The influence of pin geometry on bonding and mechanical properties in friction stir weld 2014 Al alloy. *Mater Lett* 59:2948–2952
- Zhao YH, Lin SB, Qu FX, Wu L (2006) Influence of pin geometry on material flow in friction stir welding process. *Mater Sci Technol* 22:45–50
- Buffa G, Hua J, Shivpuri R (2006) Design of the friction stir welding tool using the continuum based FEM model. *Mater Sci Eng A* 419:381–388
- Fujii H, Cui L, Maeda M (2006) Effect of tool shape on mechanical properties and microstructure of friction stir welded aluminum alloys. *Mater Sci Eng A* 419:25–31
- Kumar K, Kailas SV (2008) The role of friction stir welding tool on material flow and weld formation. *Mater Sci Eng A* 485:367–374
- Colegrove PA, Shercliff HR (2004) Development of Trivex friction stir welding tool. Part 1—two-dimensional flow modeling and experimental validation. *Sci Technol Weld Join* 9:345–351
- Colegrove PA, Shercliff HR (2004) Development of Trivex friction stir welding tool. Part 2—three-dimensional flow modeling. *Sci Technol Weld Join* 9:352–361
- Colegrove PA, Shercliff HR (2005) 3-Dimensional CFD modeling of flow round a threaded friction stir welding tool profile. *J Mater Process Technol* 169:320–327
- Sorensen CD, Stahl AL (2007) Experimental measurement of load distributions on friction stir weld pin tools. *Metall Mater Trans B* 38B:451–459
- Arora A, De A, DebRoy T (2011) Toward optimum friction stir welding tool shoulder diameter. *Scr Mater* 64:9–12

20. Mehta M, Arora A, De A, DebRoy T (2011) Tool geometry for friction stir welding—optimum shoulder diameter. *Metall Mater Trans A*. 42A:2716–2722
21. Popov EP (2003) *Engineering mechanics of solids*, 2nd edn. Pearson Education, New Delhi, sections 10.9, 11.4 and 13.10
22. Arora A, Nandan R, Reynolds AP, DebRoy T (2009) Torque, power requirement and stir zone geometry in friction stir welding through modeling and experiments. *Scr Mater* 60:13–16
23. Arora A, Zhang Z, De A, DebRoy T (2009) Strain and strain rates during friction stir welding. *Scr Mater* 61:863–866
24. Nandan R, Roy GG, Lienert TJ, DebRoy T (2006) Numerical modeling of 3D plastic flow and heat transfer during friction stir welding of stainless steel. *Sci Technol Weld Join* 11:526–537
25. Nandan R, Roy GG, DebRoy T (2006) Numerical simulation of three-dimensional heat transfer and plastic flow during friction stir welding. *Metall Mater Trans A* 37A:1247–1259
26. Nandan R, Roy GG, Lienert TJ, DebRoy T (2007) Three-dimensional heat and material flow during friction stir welding of mild steel. *Acta Mater* 55:883–895
27. Nandan R, Prabu B, De A, DebRoy T (2007) Improving reliability of heat transfer and materials flow calculations during friction stir welding of dissimilar aluminum alloys. *Weld J* 86:313s–322s
28. Nandan R, Lienert TJ, DebRoy T (2008) Toward reliable calculations of heat and plastic flow during friction stir welding of Ti–6Al–4V alloy. *Int J Mater Res* 99:434–444
29. Li Q, Lovell M (2005) On the critical interfacial friction of a two-roll CWR process. *J Mater Proc Technol* 160:245–256
30. Yan JH, Sutton MA, Reynolds AP (2005) Process–structure–property relationship for nugget and heat affected zone regions of AA2524-T351 friction stir welds. *Sci Technol Weld Join* 10:725–736
31. Boyles J (2008) Process development for and property evaluation of friction stir welded titanium alloys. Dissertation, University of South Carolina, Columbia
32. Shi Q (2002) Prediction of thermal distortion and thermal fatigue in shot sleeves. Dissertation, The Ohio State University, Columbus
33. Gan W, Li ZT, Khurana S (2007) Tool material selection for friction stir welding of L80 steel. *Sci Technol Weld Join* 12:610–613
34. Kravchenko VS, Sheina IV, Gnuchev VS, Zashimchuk EE, Kharchenko VK, Vashchenko AN (1979) Temperature dependence of the yield strength of tungsten with different microstructures. *Strength Mater* 11:175–178
35. Nielsen B (2009) Developing response surfaces based on tool geometry for a convex scrolled shoulder step spiral (CS4) friction stir processing tool used to weld AL 7075. Dissertation, Brigham Young University, Provo